A Model for Saturated-Unsaturated Flow with Fractures Acting as Capillary Barriers

Jhabriel Varela[1], Eirik Keilegavlen[1], Jan M. Nordbotten[1], and Florin A. Radu[1]

[1]Affiliation not available

August 4, 2023

Core ideas:

1. Due to the presence of air in dry fractured soils, fractures of large aperture act as capillary barriers to water flow.
2. If the capillary barriers are overcome, fractures become fast-flowing paths for water to travel downward.
3. A model for flow in fractured soils based on Richards' equation in the soil and instantaneous ponding in the fractures is proposed.
4. The model is numerically consistent, and its physical applicability is showcased in two-dimensional simulations.

A Model for Saturated-Unsaturated Flow with Fractures Acting as Capillary Barriers

Jhabriel Varela[1, *], Eirik Keilegavlen[1], Jan M. Nordbotten[1], Florin A. Radu[1]

[1] Center for Modeling of Coupled Subsurface Dynamics, Department of Mathematics, University of Bergen, P.O. Box 7800, N-5020 Bergen, Norway.

Corresponding author *: jhabriel.varela@uib.no

DFN, Discrete Fracture Network; DFM, Discrete Fracture Matrix; MPFA, Multi-Point Flux Approximation; ODE, Ordinary Differential Equation; PDE, Partial Differential Equation

ABSTRACT

In this paper, we present a model for saturated-unsaturated flow in fractured soils using an explicit representation of the fractures. The model is based on Richards' equation in the matrix and hydrostatic equilibrium in the fractures. While the first modeling choice is standard, the latter is motivated by the difference in flow regimes between matrix and fractures, i.e., the water velocity inside the fractures is considerably larger than in the soil even under saturated conditions. On matrix/fracture interfaces, the model permits water exchange between matrix and fractures only when the capillary barrier offered by the presence of air inside the fractures is overcome. Thus, depending on the wetting conditions, fractures can either act as impervious barriers or as paths for rapid water flow. Since in numerical simulations each fracture face in the computational grid is a potential seepage face, solving the resulting system of non-linear equations is a non-trivial task. Here, we propose a general framework based on a discrete-fracture matrix approach, a finite volume discretization of the equations, and a practical iterative technique to solve the conditional flow at the interfaces. Numerical examples support the mathematical validity and the physical applicability of the model.

Keywords: Richards' equation, unsaturated fractured flow, capillary barrier, discrete fracture matrix, mixed-dimensional geometry.

1 INTRODUCTION

Improving our understanding of how water flows in the vadose zone is highly relevant for a wide variety of processes such as water management, support of plants via evapotranspiration, transport of nutrients, soil remediation, and nuclear waste disposal (Šimůnek & Bradford, 2008). The simultaneous flow of water and air in the unsaturated zone is usually modeled by Richards' equation (Richards, 1931), where the air is considered inviscid and its pressure equal to the atmospheric pressure, thus only the equations corresponding to the water phase have to be taken into account (Pinder & Celia, 2006).

Although Richards' equation has been extensively studied for non-fractured domains (Farthing & Ogden, 2017), models for unsaturated fractured flow are far less developed. In fact, much of the understanding of unsaturated fractured systems took place in the late 1970s and early 1980s, when the US Department of Energy began to consider the possibility of storing spent nuclear fuel and high-level radioactive waste in the Yucca Mountain in southern Nevada (Macfarlane & Ewing, 2006).

In their seminal paper, Wang and Narasimhan (1985) provide an insightful description of the hydrological mechanisms that govern unsaturated fractured flow. In these systems, the presence of air in the fractures completely changes the flow dynamics relative to the fully saturated case since the continuity of the liquid phase at the matrix/fracture interface is either partially or entirely lost. Indeed, continuity is preserved only in regions of small fracture aperture, where capillary forces can still "hold" the liquid phase, providing a connection of reduced contact area between the adjacent matrix blocks. However, in regions of large aperture,

this no longer occurs, and the non-wetting phase acts as an impervious barrier to liquid flow in the direction parallel to the fracture. This barrier is often referred to as a *capillary barrier*.

Two approaches are commonly employed for representing fractures in mathematical models (Berre et al., 2019; Formaggia et al., 2021): (1) equivalent continuum-type models, and (2) models explicitly representing fractures. In the first approach, matrix and fracture are represented as a single continuum or, alternatively, as multiple continua coupled through transfer terms. In the second approach, fractures are represented as separate objects embedded in the matrix. Fracture and matrix are then linked through coupling conditions. Prototypical examples of continuum models include the dual porosity and dual permeability models, whereas models representing the fractures explicitly include the Discrete Fracture Matrix (DFM) and Discrete Fracture Network (DFN) models. Referring to the unsaturated case, both types of representations have been proven useful. See, for example (Brouyère, 2006; Chen et al., 2022; Kordilla et al., 2012; Kuráž et al., 2010; Robineau et al., 2018; Spiridonov et al., 2020) for continuum-type models, and (Koohbor et al., 2020; Li & Li, 2019; Therrien & Sudicky, 1996; Tran & Matthai, 2021) for models explicitly representing the fractures.

Most current models for saturated-unsaturated fractured flow are based on the hypothesis that the continuity of the liquid phase is preserved (at least in some average sense) and employ a Richards-like process to describe the flow inside the fracture. Experimental evidence suggests, however, that for fractures of sufficiently large aperture, water moves downward in the form of thin films due to the action of the gravity (Dragila & Wheatcraft, 2001; Tokunaga & Wan, 1997; Tokunaga et al., 2000; Wang et al., 2013). More importantly, the average downward velocity of such films usually surpasses the velocity in the matrix under saturated conditions (Su et al., 2003; White, 2006).

Motivated by these experimental observations, we consider the limiting case where fractures are considered infinitely conductive and propose a model where water ponds instantaneously rather than traveling with finite speed inside the fractures. This idealization is justifiable for short fractures (where there is a short travel time) with large apertures embedded in soils of low conductivity (thus the contrast between regimes is large). We remark that a similar type of model was derived using formal and rigorous upscaling. See, in particular, the Effective Model III obtained by List et al. (2020) and the Effective Model VIII from Kumar et al. (2020).

Below, we make precise our modeling principles based on an DFM representation of the fractures:

MP1. In the matrix, the flow of water is governed by Richards' equation.

MP2. Any amount of water entering a fracture (or fracture network) travel downward without resistance and is instantaneously in hydrostatic equilibrium.

MP3. Flow of water across the fracture/matrix interface can only occur if the capillary barrier is overcome. Otherwise, the fracture/matrix interface is impervious to water flow.

Based on these modeling principles, our proposed model can be mathematically classified as a PDE/ODE system of equations with variational inequalities. The PDE part is related to Richards' equation in the matrix (MP1), the ODE part is related to the volume balance in the fractures (MP2), and the variational inequalities consider the conditional flow due to the presence of capillary barriers (MP3).

Thus far, we have only discussed the effect of a single isolated fracture. However,

fractures can be interconnected as part of a fracture network. Naturally, this poses an additional layer of complexity in terms of modeling and implementation since we must consider the water redistribution problem inside the network. Our aim is to show that this challenge can be tackled with a robust description of the fracture networks based on a mixed-dimensional decomposition (Boon et al., 2021; Boon et al., 2018), an appropriate choice of primary variables, and the application of iterative solution strategies.

The rest of the paper is organized as follows: In Section 2, we introduce the model problem for the case of a single vertical embedded in a matrix. In Section 3, we extend the single fracture model to account for networks of fractures and briefly discussed the solution strategy. Finally, in Section 4, we present our numerical examples, and in Section 5 draw our conclusions.

2 THE MODEL FOR A SINGLE FRACTURE

In this section, we derive the model based on physical principles for the case of a single fracture embedded in a matrix. Throughout this paper, we use $\boldsymbol{x} = [x,\ z] \in \mathbb{R}^2$, to denote the vector of spatial coordinates, with z referring to the vertical coordinate, which is taken positively with an upward-pointing direction. Moreover, we let t denote the time, with $T > 0$ representing the final time, and $(0, T)$ the time interval of interest. Central to our vocabulary is the concept of hydraulic head: $h = \psi + \zeta$, with ψ denoting the pressure head, and ζ the elevation head (Pinder & Celia, 2006). For the sake of simplicity, here, we assume $\zeta = z$.

Let us now consider a domain $Y \subset \mathbb{R}^2$ decomposed into a matrix Ω_b and a single fully embedded vertical fracture Ω_f such that $Y = \Omega_f \sqcup \Omega_b$, as depicted in the left panel of Figure 1. We let Γ_+ and Γ_- be the interfaces between Ω_b and the left and right sides of Ω_f, respectively

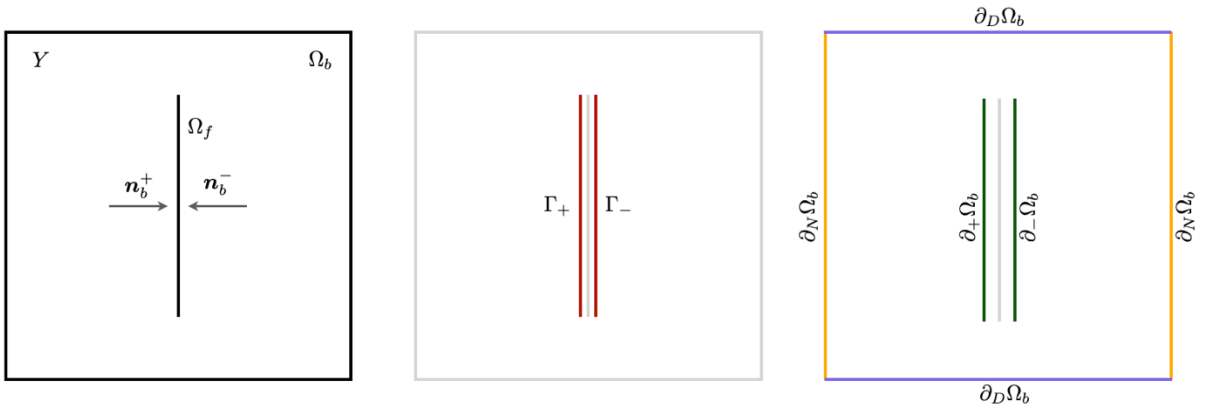

Figure 1: Geometric entities. Left: A one-dimensional fracture Ω_f fully embedded in the two-dimensional matrix Ω_b. Center: Interfaces Γ_+ and Γ_- establish the link between Ω_f and Ω_b. Right: Internal ($\partial_+\Omega_b$ and $\partial_-\Omega_b$) and external ($\partial_D\Omega_b$ and $\partial_N\Omega_b$) boundaries. Note that in practice $\partial_+\Omega_b$, Γ_+, Ω_f, Γ_-, and $\partial_-\Omega_b$, all coincide spatially. For illustrative purposes, however, they are drawn in different locations.

(see the center panel of Figure 1). Finally, we introduce the internal boundaries $\partial_+\Omega_b$ and $\partial_-\Omega_b$ (see the right panel of Figure 1), which are defined to spatially coincide with Γ_+ and Γ_-.

2.1 Governing equations in the matrix

We start by presenting the governing equations in the matrix, where we consider that the water flow can be described by Richards' equation following MP1. The set of governing equations in Ω_b then reads:

$$\frac{\partial \theta_b}{\partial t} + \boldsymbol{\nabla} \cdot \boldsymbol{q}_b = \Psi_b, \qquad \text{in } \Omega_b \times (0,T), \tag{1}$$

$$\boldsymbol{q}_b = -\boldsymbol{K}_b k_b^{\mathrm{rel}} \boldsymbol{\nabla} h_b, \qquad \text{in } \Omega_b \times (0,T), \tag{2}$$

$$\boldsymbol{q}_b \cdot \boldsymbol{n}_b = \lambda_{\pm}, \qquad \text{on } \partial_{\pm}\Omega_b \times (0,T), \tag{3}$$

$$\boldsymbol{q}_b \cdot \boldsymbol{n}_b = g_{N,b}, \qquad \text{on } \partial_N\Omega_b \times (0,T), \tag{4}$$

$$h_b = g_{D,b}, \qquad \text{on } \partial_D\Omega_b \times (0,T), \tag{5}$$

$$h_b = g_{0,b}, \qquad \text{in } \Omega_b \times \{0\}. \tag{6}$$

Here, (1) is the mass conservation equation, where $\theta_b := \theta(\psi_b)$ is the matrix water content, $\boldsymbol{q}_b$ is the matrix Darcy's flux, and Ψ_b is an external volumetric source (or sink) of water. The flux

$\boldsymbol{q}_b$ is given by the multiphase version of Darcy's law (2), where $\boldsymbol{K}_b$ is the hydraulic conductivity tensor under saturated conditions, h_b is the matrix hydraulic head, and $k_b^{\mathrm{rel}} \coloneqq k^{\mathrm{rel}}(\psi_b)$ is the water relative permeability. We precisely define θ_b and k_b^{rel} in Section 2.4.

Equations (3) enforce normal fluxes on the internal boundaries to match the interface fluxes $\lambda_{\pm}$, which are included as additional unknowns and will be defined later. By construction, we require the normal vectors $\boldsymbol{n}_b$ on internal boundaries pointing from Ω_b to Ω_f (see the left panel of Figure 1). Moreover, (4) and (5) impose flux and constant head boundary conditions, where $g_{N,b}$ is a prescribed outer normal flux across $\partial_N\Omega_b$, and $g_{D,b}$ is a prescribed hydraulic head on $\partial_D\Omega_b$. Finally, (6) establishes an initial hydraulic head distribution.

2.2 Volume balance in the fracture

Following our assumption of instantaneous hydrostatic equilibration (MP2), the equations in the fracture are given by the following initial value problem:

$$\frac{\mathrm{d}V_f}{\mathrm{d}t} = \int_{\Omega_f} (\lambda_+ + \lambda_-)\,\mathrm{d}\boldsymbol{x} + \int_{\Omega_f} \Psi_f\,\mathrm{d}\boldsymbol{x}, \qquad \text{in } \Omega_f \times (0,T), \tag{7}$$

$$h_f = g_{0,f}, \qquad \text{in } \Omega_f \times \{0\}. \tag{8}$$

Equation (7) describes the volumetric changes of water in Ω_f. It requires the rate of change of water volume $V_f = V(h_f)$ in Ω_f to balance the water exchanged with Ω_b via the interface fluxes $\lambda_{\pm}$ plus external sources (or sinks) of water Ψ_f. The term Ψ_f can be employed to mimic direct infiltration or evaporation in the fractures. The precise relationship between V_f and the hydraulic head in the fracture h_f will be given in Section 2.4. Finally, in (8), we specify an initial hydraulic head in the fracture.

2.3 Interface fluxes

On the interfaces $\Gamma_{\pm}$, we consider that the interface fluxes $\lambda_{\pm}$ depend on the hydraulic heads of the fracture h_f and the surrounding matrix h_b. Thus, extending upon the work of Martin et al. (2005) and Ahmed et al. (2017) to account for the conditional flow due to the capillary barriers (MP2), the interface fluxes are given by:

$$\lambda_{\pm} = -\gamma_{\pm} \frac{2\kappa_{\pm}}{a_f} k_{\pm}^{\mathrm{rel}} \left(h_f - h_b\right), \qquad \text{on } \Gamma_{\pm} \times (0,T), \tag{9}$$

$$\lambda_{\pm} = \lambda_{0,\pm}, \qquad \text{on } \Gamma_{\pm} \times \{0\}. \tag{10}$$

In (9), $\kappa_{\pm}$ are the normal hydraulic conductivities under saturated conditions, a_f is the fracture's aperture, $\gamma_{\pm}$ are threshold functions that allow (or prevent) the flux across the interfaces based on neighboring wetting conditions, and $k_{\pm}^{\mathrm{rel}}$ are the relative permeabilities on the interfaces. In Section 2.4, we make $\gamma_{\pm}$ and $k_{\pm}^{\mathrm{rel}}$ precise. Finally, (10) establishes initial interface fluxes.

2.4 Constitutive relationships and closure conditions

To close the system of equations, we need constitutive relationships for the matrix, fracture, and interfaces. As is accustomed for the vadose zone, we employ the van Genuchten-Mualem relations (Mualem, 1976; Van Genuchten, 1980):

$$\theta(\psi) = \begin{cases} \theta^{\mathrm{res}} + (\theta^{\mathrm{sat}} - \theta^{\mathrm{res}})[1 + (\alpha_{\mathrm{vG}}|\psi|^{n_{\mathrm{vG}}})]^{\frac{1}{n_{\mathrm{vG}}}-1}, & \psi < 0, \\ \theta^{\mathrm{sat}}, & \psi \geq 0, \end{cases} \tag{11}$$

$$\Theta(\psi) = \frac{\theta(\psi) - \theta^{\mathrm{res}}}{\theta^{\mathrm{sat}} - \theta^{\mathrm{res}}}, \tag{12}$$

$$k^{\mathrm{rel}}(\psi) = \sqrt{\Theta(\psi)} \left\{1 - \left[\left(1 - \Theta(\psi)\right)^{\frac{n_{\mathrm{vG}}}{n_{\mathrm{vG}}-1}}\right]\right\}^2. \tag{13}$$

Here, a_{vG}, and n_{vG} are model parameters that depend on the type of soil, θ^{res} and θ^{sat} are, respectively, the water content under residual and saturated conditions, and Θ is the effective

161 saturation.

162 In the fracture, we need to relate the water volume V_f with the hydraulic head h_f. In the
163 most general case where the aperture can vary in space, this relationship is given by the
164 following volume integral:

$$V_f = \int_{\substack{\Omega_f \\ z<h_f}} a_f \, \mathrm{d}\boldsymbol{x}. \tag{14}$$

165 Let us now focus on the interfaces. We note that the interface fluxes $\lambda_\pm$ must be zero
166 unless the capillary barrier is exceeded. This motivates defining the Heaviside functions $\gamma_\pm$ as:

$$\gamma_\pm(\psi_b, \psi_f, \psi_L) = \begin{cases} 1, & \psi_b > \psi_L \\ 1, & \psi_f > \psi_L \\ 0, & \text{otherwise} \end{cases}, \quad \text{on } \Gamma_\pm \times (0,T), \tag{15}$$

167 where ψ_L is the pressure threshold, i.e., the minimum pressure head necessary to break the
168 capillary barrier. Although there exists experimental evidence suggesting $\psi_L < 0$ (Tokunaga &
169 Wan, 2001) for different types of soils, in this paper, we require reaching saturation conditions to
170 break the capillary barrier. Thus, from this point forward, we assume $\psi_L = 0$.

171 Finally, a concrete value for $k_\pm^{\mathrm{rel}}$ can be obtained via a semi-discrete inter-dimensional
172 potential-based upstream weighting (Chen et al., 2006):

$$k_\pm^{\mathrm{rel}}(\psi_b, \psi_f) = \begin{cases} k^{\mathrm{rel}}(\psi_b), & \psi_b > \psi_f \\ k^{\mathrm{rel}}(\psi_f), & \psi_b \leq \psi_f \end{cases}, \quad \text{on } \Gamma_\pm \times (0,T). \tag{16}$$

173 Equations (1) to (16) represent a closed system of non-linear differential equations with
174 h_b, h_f, and $\lambda_\pm$ as primary variables.

175 **3 GENERAL MODEL AND SOLUTION STRATEGY**

The aim of this section is to generalize the single fracture model to account for networks of fractures. The extension is non-trivial, as it requires modeling of fluid transport within the fracture network accounting for fracture intersections. Key to the modeling is a description of the mixed-dimensional decomposition of the domain, which we present in a general form whereupon we write the general model. Finally, we briefly discuss some aspects related to the solution strategy.

3.1 Mixed-dimensional geometric decomposition

To extend the model of a single fracture to a more general setting, we first need to introduce the mixed-dimensional geometric decomposition of the domain. The formulation follows the one originally proposed by Boon et al. (2018) and more closely the one recently employed by Varela et al. (2022). First, consider a domain $Y \subset \mathbb{R}^2$, decomposed into m subdomains Ω_i of dimension $d_i = d(i)$ so that $Y = \cup_{i \in I} \Omega_i$, with $I = 1, \dots, m$. We assume that all subdomains of dimensions d_i are disjoint. In practice, $d_i = 2$ represents the soil, $d_i = 1$ the fractures, and $d_i = 0$ the intersection between fractures.

Having seen the utility of defining a distinct object to pose equations at both sides of the fracture, now, we generalize it by allowing subdomains one-dimension-apart to be coupled via interfaces Γ_j, for $j \in J$, where $J = 1, \dots, M$, with M denoting the total number of interfaces. More precisely, for a given interface Γ_j, we use $\Omega_{\hat{\jmath}}$ for $\hat{\jmath} \in I$ and $\Omega_{\check{\jmath}}$ for $\check{\jmath} \in I$, to denote its higher- and lower-dimensional neighboring subdomain. The internal boundary of $\partial_j \Omega_{\hat{\jmath}}$ of $\Omega_{\hat{\jmath}}$ is defined such that it coincides with Γ_j; which, in turn, matches with the lower-dimensional neighbor $\Omega_{\check{\jmath}}$.

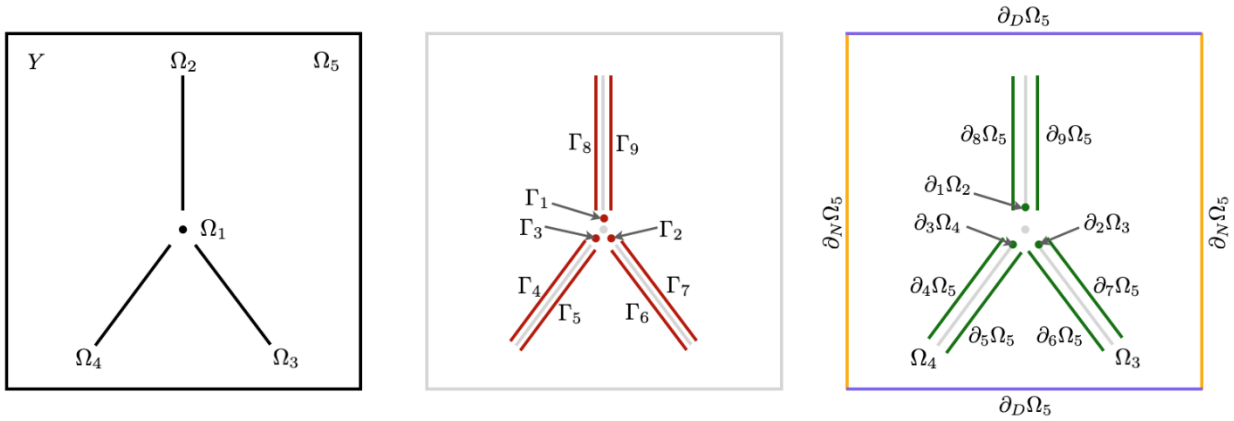

Figure 2: Mixed-dimensional geometric decomposition showing subdomains, interfaces, and boundaries for the case of a matrix Ω_5 hosting three fractures $(\Omega_2, \Omega_3, \Omega_4)$ intersecting in a common point Ω_1.

Unlike the model with a single fracture, now a different number of interfaces can be linked to a single subdomain. Thus, to establish the communication between subdomains and interfaces in a more general way, we introduce the index sets $\hat{S}_i$ and $\check{S}_i$, containing the indices of the higher- and lower-dimensional neighboring interfaces of Ω_i, respectively. To provide concrete examples of such sets, consider Figure 2, where we show the mixed-dimensional decomposition for the case of three fractures embedded in a matrix which intersect in a common point. If we take, for example, the subdomain Ω_4, it is straightforward to see that $\hat{S}_4 = \{4, 5\}$, whereas $\check{S}_4 = \{3\}$.

Finally, we consider the decomposition of the boundaries of Ω into its Dirichlet, Neumann, and internal parts: $\partial\Omega = \partial_D\Omega \cup \partial_N\Omega \cup \partial_\jmath\Omega$, where $\partial_D\Omega = \cup_{i\in I}\, \partial_D\Omega_i$, $\partial_N\Omega = \cup_{i\in I}\, \partial_N\Omega_i$, and $\partial_\jmath\Omega = \cup_{i\in I}\cup_{j\in\hat{S}_i}\, \partial_j\Omega_i$.

3.2 The general model

Extending the single-fracture model to account for a fracture network is now

straightforward up to the treatment of intersections, which will be devoted special attention. Below, we make precise the complete set of equations valid for all subdomains Ω_i with $i \in I$, and all interfaces Γ_j with $j \in J$.

3.2.1 Conservation laws

The conservation laws on subdomains can be summarized by the following equations:

$$\frac{\partial \theta_i}{\partial t} + \boldsymbol{\nabla} \cdot \boldsymbol{q}_i - \Psi_i = 0, \qquad \text{in } \Omega_i \times (0,T), \qquad d_i = 2, \tag{17}$$

$$\frac{\mathrm{d}V_i}{\mathrm{d}t} - \int_{\Omega_i} \sum_{j \in \hat{S}_i} \lambda_j \, \mathrm{d}\boldsymbol{x} - \int_{\Omega_i} \Psi_i \, \mathrm{d}\boldsymbol{x} = 0, \qquad \text{in } \Omega_i \times (0,T), \qquad d_i = 1, \tag{18}$$

$$\sum_{j \in \hat{S}_i} \lambda_j = 0, \qquad \text{in } \Omega_i \times (0,T), \qquad d_i = 0. \tag{19}$$

Equation (17) has the same form as (1), with the exception that we now allow for more than one matrix subdomain. Equation (18) governs the volume balance in each fracture and thus generalizes (7). Finally, (19) requires all fluxes entering an intersection point to match the fluxes leaving the same intersection point. Due to the negligible volume associated with points, we do not associate any volume to them and thus explicitly remove accumulation and source terms from (19). Note, however, that there is still a well-defined hydraulic head associated to zero-dimensional subdomains.

3.2.2 Darcy-type laws

The constitutive laws relating fluxes with changes in hydraulic heads are given by:

$$\boldsymbol{q}_i + \boldsymbol{K}_i k_i^{\mathrm{rel}} \boldsymbol{\nabla} h_i = 0, \qquad \text{in } \Omega_i \times (0,T), \qquad d_i = 2, \tag{20}$$

$$\lambda_j + \gamma_j \frac{2\kappa_j}{a_j} k_j^{\mathrm{rel}} \left(h_j - h_j\right) = 0, \qquad \text{on } \Gamma_j \times (0,T), \qquad d_j = 1, \tag{21}$$

$$\lambda_j + \gamma_j \kappa_\tau \left(h_j - h_j\right) = 0, \qquad \text{on } \Gamma_j \times (0,T), \qquad d_j = 0. \tag{22}$$

Equation (20) has again the same form as (2). Similarly, but for interfaces, (21) has the same form as (9). The zero-dimensional interface fluxes are given by (22). Note that these fluxes are the ones entering the conservation law (19).

The hydrostatic equilibrium condition (MP2) now applies to the whole fracture network rather than to individual fractures. In a continuous sense, this implies that the interface fluxes λ_j in (22) must transfer water from fractures of high elevation to connected branches of lower elevation *infinitely* fast (e.g., from Ω_2 to Ω_3 and Ω_4 referring to Figure 2). Otherwise, we would have "floating" water columns sitting on top of intersection points, which is clearly unphysical. In practice, however, we only need to guarantee hydrostatic equilibrium *in-between* time steps. This can be achieved by ensuring sufficiently large values of λ_j with the computational parameter κ_τ. We discuss this implementational aspect with more detail in Section 3.3.

3.2.3 Boundary and initial conditions

The model is completed by providing internal and external boundary conditions together with initial conditions:

$$\boldsymbol{q}_{\hat{\jmath}} \cdot \boldsymbol{n}_{\hat{\jmath}} - \lambda_j = 0, \quad \text{on } \partial_j\Omega_{\hat{\jmath}} \times (0,T), \quad d_j = 1, \tag{23}$$

$$\boldsymbol{q}_i \cdot \boldsymbol{n}_i - g_{N,i} = 0, \quad \text{on } \partial_N\Omega_i \times (0,T), \quad d_i = 2, \tag{24}$$

$$h_i - g_{D,i} = 0, \quad \text{on } \partial_D\Omega_i \times (0,T), \quad d_i = 2, \tag{25}$$

$$h_i - g_{0,i} = 0, \quad \text{on } \Omega_i \times \{0\}, \quad d_i = 0,1,2, \tag{26}$$

$$\lambda_j - \lambda_{0,j} = 0, \quad \text{on } \Gamma_j \times \{0\}, \quad d_j = 0,1. \tag{27}$$

Naturally, the model should also be complemented with the closure relations from Section 2.4, which are still valid for the case of fracture networks.

3.3 Solution strategy

240 The set of equations (17) to (27) is discretized using backward Euler in time and cell-
241 centered finite volumes in space. More precisely, we employ the multipoint flux approximation
242 MPFA-O method. We refer the reader to (Aavatsmark, 2002; Nordbotten & Keilegavlen, 2021)
243 for the details on the MPFA method. For linearizing the set of non-linear equations, we employ
244 the modified Picard iteration (Celia et al., 1990) in the matrix and the Newton method in the
245 fractures. For a thorough review on linearization techniques for Richards' equation, we refer to
246 (List & Radu, 2016).

247 To solve the conditional flow on the interfaces, that is, to obtain γ_j, we use an iterative
248 approach like those employed in seepage analysis (Scudeler et al., 2017). The algorithm is
249 simple: At a given time level, we set $\gamma_j = 0$ for all interface cells (recall that this makes the cells
250 impervious to flow). Then, we proceed to solve the system of equations until convergence and
251 review if the pressure head in some of the interface cells is greater than 0. If so, the interface cell
252 is assigned $\gamma_j = 1$, and the solution is recomputed with the updated conditions. Otherwise, we
253 directly proceed to the next time level. In Figure 3, we show the possible flow scenarios during a
254 hypothetical irrigation process. Instead of employing an iterative approach, one can use
255 regularization techniques (Trémolières et al., 2011), where the Heaviside function γ_j from (15) is
256 replaced by a smooth function (Chan & Vese, 2001), which admits a derivative. This technique
257 allows for solving the set of equations fully implicitly. However, one must carefully select the
258 regularization parameter to avoid nonphysical results, e.g., water leakage into the fracture below
259 the pressure threshold.

260 As we mentioned in Section 3.2.2, in the case of fracture networks, we need to ensure
261 zero-dimensional interface fluxes (e.g., λ_j from Eq. (22)) to be sufficiently large so that

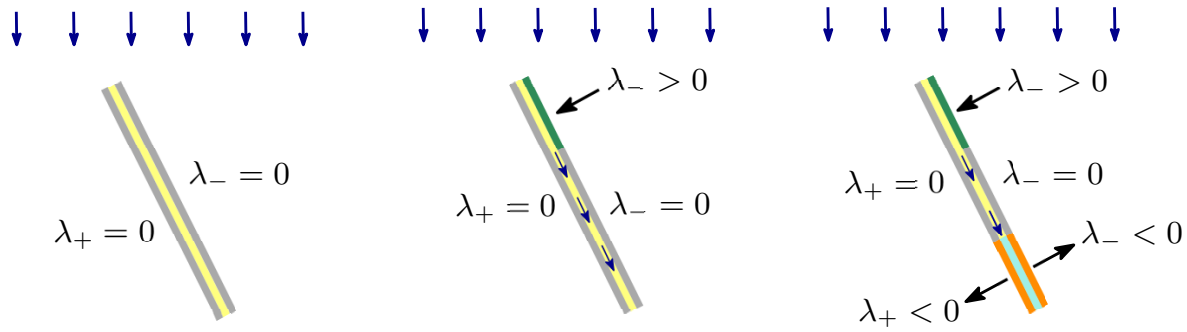

Figure 3: Possible flow scenarios during a hypothetical irrigation process for an initially dry fracture. Left: The flow across the interfaces is zero since the capillary barrier (gray) has not been exceeded. Center: On the green portion of the negative side of the interface, the capillary barrier is overcome, resulting in water entering the fracture and ponding instantaneously. Right: A pond was formed (turquoise), and water can now escape via the orange portions at both sides of the fracture. Note that imbibition still takes place through the green portion. The green and orange portions of $\Gamma_\pm$ correspond to $\gamma_\pm = 1$, whereas the gray portions to $\gamma_\pm = 0$.

hydrostatic is achieved in the whole fracture network before proceeding to the next time step τ. To this aim, we employ the computational parameter κ_τ to control the magnitude of λ_j. The precise value of κ_τ is not important, and any $\kappa_\tau \gg \tau^{-1}$ will suffice as an approximation of the equilibrium condition. The importance of equations (19) and (22) for the general model is therefore two-fold: (a) it ensures hydrostatic equilibrium in the fracture network, and (b) it distributes water among connected branches based on the difference in hydraulic heads. Alternatively, one could omit (19) and (22) altogether, use zero-dimensional subdomains as bifurcation (or mixing) points, and explicitly enforce hydrostatic equilibrium using a water re-distribution algorithm in an extra equilibration step. Both approaches should result in the same hydraulic states.

Finally, the large gradients in hydraulic head during infiltration (either from the soil surface or across the fracture faces) poses severe computational restrictions. The situation is only exacerbated in heterogeneous and layered soils. To deal with this challenge, we rely heavily on

an iteration-based time-stepping algorithm. The algorithm closely resembles the one employed in HYDRUS-1D (Šimůnek et al., 2005) and is provided in Appendix B.

4 NUMERICAL EXAMPLES

In this section, we present numerical examples that showcase the validity and applicability of the proposed model. The examples include a numerical convergence analysis and two simulations mimicking irrigation scenarios. All examples are implemented in the open-source software `PorePy` (Keilegavlen et al., 2021) using the extension package `unsat-frac` (Varela, 2023). Material parameters used in Sections 4.2 and 4.3 are given in Table 1. Unless otherwise stated, the aperture for all fractures is assumed constant and equal to 0.1 [cm].

Table 1: Physical parameters used for the soils used in the numerical examples.

Soil	$\boldsymbol{K}$ **[cm h^{-1}]**	$\boldsymbol{\theta^{sat}}$ **[−]**	$\boldsymbol{\theta^{res}}$ **[−]**	$\boldsymbol{\alpha_{vG}}$ **[cm^{-1}]**	$\boldsymbol{n_{vG}}$ **[−]**
Sand[a]	33.19	0.368	0.102	0.0335	2.00
Sandy clay[b]	0.12	0.380	0.100	0.0270	1.23
Sandy loam[b]	4.42	0.41	0.065	0.075	1.89
Sandy clay loam[b]	1.31	0.39	0.100	0.059	1.48
Loamy sand[b]	14.59	0.41	0.057	0.124	2.28

[a]Retrieved from Celia et al. (1990).

[b]Retrieved from Carsel and Parrish (1988).

4.1 Convergence analysis

For our first numerical example, we perform a convergence analysis for the case of a single vertical line Ω_1 fully embedded in a unit square Ω_2, coupled via the interfaces Γ_1 and Γ_2 to the left and right of the fracture, respectively.

Following closely Varela et al. (2022), we assume the existence of a piecewise hydraulic

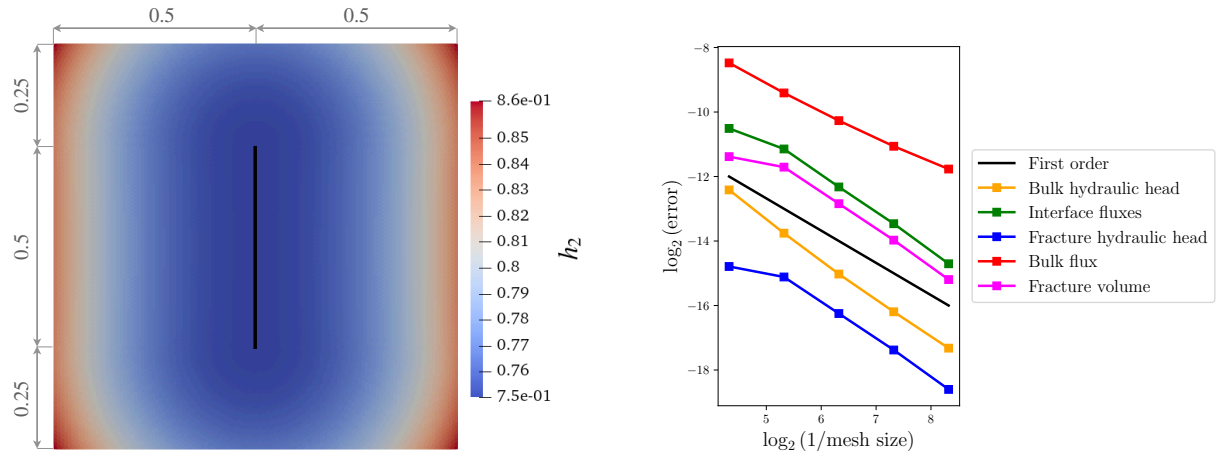

Figure 4: Exact hydraulic head in the bulk for the final simulation time (left) and convergence rates for primary and secondary variables (right). First order convergence is reported for all variables.

head distribution in the bulk h_2 (we refer to Appendix C for the derivation of all relevant quantities for this analysis), from where all other variables of interest can be derived. In the left panel of Figure 4, we show the geometric setup and the exact solution hydraulic head distribution in the matrix for the final simulation time.

Assuming initially dry conditions for the fracture, the choice of h_2 implies that for $t > 0$, both interfaces are conductive (i.e., $\gamma_1 = \gamma_2 = 1$), with water moving from the matrix to the fracture. For this analysis, we study the time interval $(0, T) = (0, 0.5)$ employing a constant time step of 0.015625. In space, we employ five levels of refinement, with target mesh sizes equal to 0.05, 0.025, 0.0125, 0.00625, and 0.003125. We investigate convergence rates of primary (i.e., $h_2, h_1, \lambda_1, \lambda_2$) and secondary variables (i.e., $\boldsymbol{q}_2$, V_1) using the discrete relative L^2-norms used in (Varela et al., 2021).

In the right panel of Figure 4, we show the errors as a function of the inverse of the mesh size. A general asymptotic first order convergence tendency is reported for all variables. This follows from the use of a first-order upwind scheme for discretizing the fluxes and is in

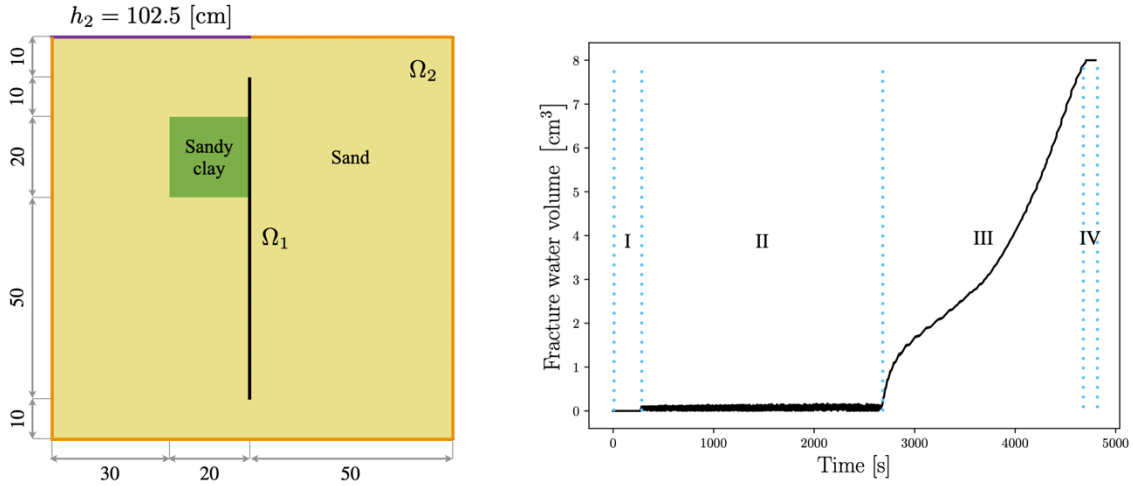

Figure 5: Geometric setup and boundary conditions for the numerical example of Section 4.2 (left) and water evolution inside the fracture (right) showcasing four distinct hydraulic stages.

agreement with previously reported rates with MPFA in simplicial grids for non-fractured domains (Klausen et al., 2008).

4.2 Infiltration into a soil with a single vertical fracture

Our second example consists of a single-one dimensional vertical fracture embedded in a squared domain as shown in the left panel of Figure 5. The yellow region corresponds to a soil sample from a New Mexico's field. A block of sandy clay (green square) is artificially located next to the fracture to enforce water accumulation on top of the block and help breaking the capillary barrier. The final simulation time is 4800 [s]. The soil is initially at moderate dry conditions with $g_{0,2} = (-500 + z_2)$ [cm]. All external boundaries are assumed to be no-flow, except for the top-left portion, where a constant head is imposed.

Figure 6 shows the hydraulic head distribution in the matrix for three different times, i.e., 336, 1680, and 3168 seconds. Water enters the domain from the top-left part of the boundary due to the difference in hydraulic heads. The wetting front is diverted by the block of sandy clay, and, as time progresses, the hydraulic head is sufficiently large to break the capillary barrier

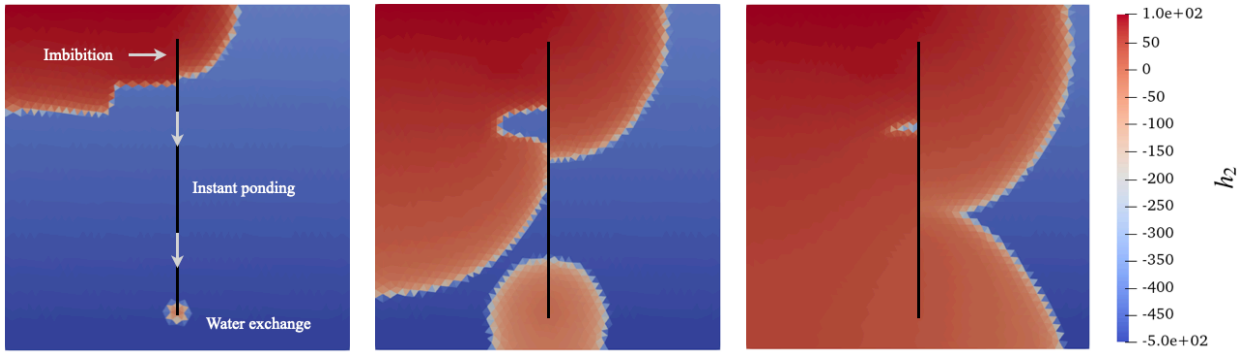

Figure 6: Simulation snapshots for three different times for the numerical example of an irrigation scenario in a soil containing a single vertical fracture.

offered by the air in the fracture. Thus, at approximately 300 [s], water enters the fracture through the faces located on top of the sandy clay block (marked by the "imbibition" label). This provides a fast-flowing path for water to travel downward. Water exchange now takes place through the bottom part of the fracture and the matrix, which, until this point, remained at dry conditions. At $t = 1680$ [s], water exchange keeps progressing through the bottom of the fracture, and, eventually, the two wetting fronts merge. Finally, at $t = 3168$ [s], almost all the domain has become saturated. Global equilibrium (not shown in the figure) is achieved at around 4800 [s] where the entire domain reaches the imposed boundary hydraulic head value of 102.5 [cm].

The right panel of Figure 6 shows the water volume evolution inside the fracture. We recognize four distinct stages. In stage I, the fracture remains at dry conditions. In stage II, water exchange takes place through the bottom of the fracture. During this stage, the volume oscillates with an amplitude of ~ 0.1 [cm^3] due to the intermittent dry/wet states of the bottom ghost fracture cell (see also Figure A.1). A more refined fracture ghost grid will result in oscillations of smaller amplitude. In stage III, the water column inside the fracture smoothly increases as a

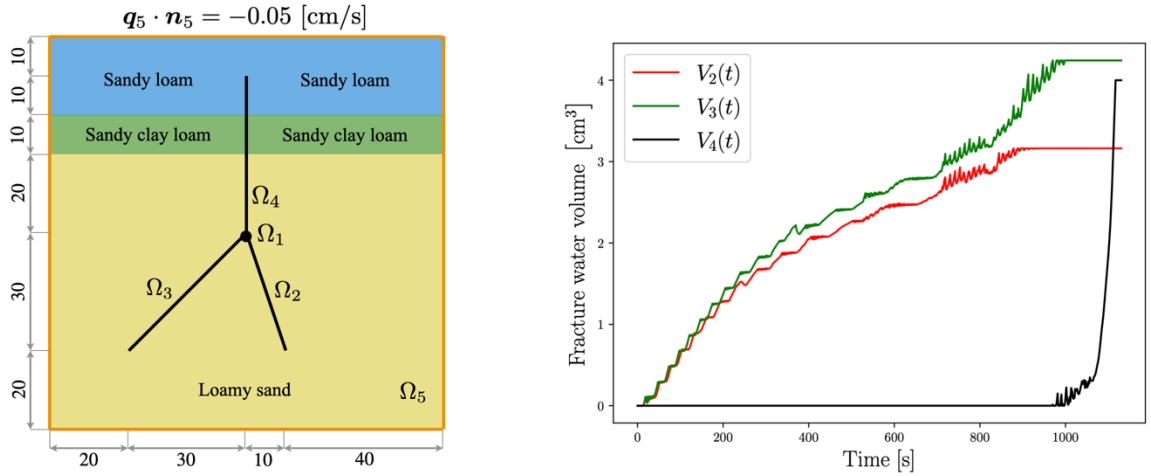

Figure 7: Geometric setup and boundary conditions for the numerical example of Section 4.3 (left) and water volume evolution inside the facture network (right).

response of the saturated conditions in the neighboring matrix. Finally, in stage IV, the fracture is entirely filled with water. Note, however, that the fracture hydraulic head might still increase e.g., due to an increase in water pressure above the fracture level. This behavior is naturally captured by our model thanks to the choice of hydraulic head (and not the water volume) as primary variable for the fracture subdomains.

4.3 Infiltration into a soil with a fracture network

Our final example considers the case of a fracture network with a junction as shown in the left panel of Figure 7. The domain is stratified with three types of loam, i.e., sandy loam (top), sandy clay loam (middle), and loamy sand (bottom). We set all external boundaries of the domain as impervious, except the top boundary where a constant infiltration velocity of 0.05 [cm/s] is prescribed. Initially, the top layer is at almost saturated conditions with $g_{0,5} = (-5 + z_5)$ [cm], whereas the middle and bottom layers are at moderate dry conditions with $g_{0,5} = (-500 + z_5)$ [cm] $+ z_5$. All fractures are initially dry, and the final simulation time is 1130 [s].

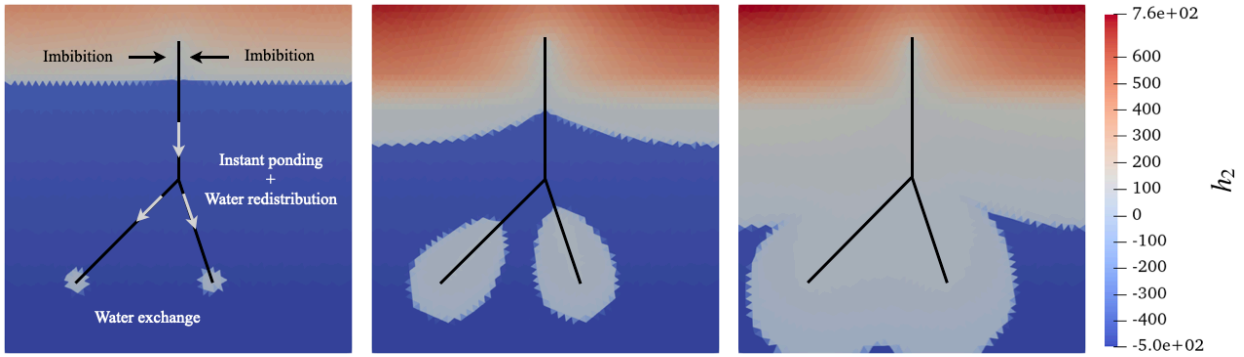

Figure 8: Hydraulic head distributions in the matrix for three different times. Water enters the top fracture through the sandy loam layer, ponds, and bifurcate through the left and right branches of the fracture network. In this case, we have employed a water distribution algorithm that equally distributes water from Ω_2 to Ω_3 and Ω_4.

In Figure 8, we show the hydraulic head distributions for three times, namely 60, 384, and 1115 [s]. At approximately 60 [s], imbibition starts taking place from both sides of the part of Ω_4 embedded in the top layer of Ω_5. The amount of water that enters, travels downward (circumventing the resistance of the sandy clay loam) and ponds instantaneously to the bottom of Ω_4 and then distributes between Ω_2 and Ω_3. At $t = 384$ [s], more water has traveled from the upper part of Ω_4 to the bottom of Ω_2 and Ω_3, and as such, larger parts of Ω_5 become wet. The irrigation front also developed significantly, saturating the top and middle layers. Finally, at $t = 1115$ [s], the wetting fronts merge and most of the domain becomes saturated.

In the right panel of Figure 7, we show the water evolution in each fracture of the fracture network. The water volumes in Ω_2 and Ω_3 consistently increase in response to larger parts of the domain becoming saturated. The fracture Ω_2 is fully filled at around 890 [s], whereas Ω_3 is filled at around 950 [s]. Only after this point, the volume of water in Ω_4 increases. Since there is no-longer water redistribution inside the network, the volume increases quite rapidly, until it reaches its maximum value at around 1110 [s].

CONCLUSION

In this paper, we have presented a new model for saturated-unsaturated flow in the presence of fractures acting as capillary barriers. The proposed model serves as a practical tool to assess the rapid movement of water through fracture networks when the capillary barrier imposed by the air inside the fractures is exceeded, which are otherwise impervious to the water flow (i.e., in the strictly unsaturated case).

A convergence analysis confirmed the numerical correctness of the model, whereas simulations have produced physically coherent results. Accounting for a more accurate description of the water flow inside the fracture network (e.g., water film flow) together with its generalization to three dimensions are natural extensions to the current model.

ACKNOWLEDGMENTS

Jhabriel Varela was funded by VISTA – a basic research program in collaboration between The Norwegian Academy of Science and Letters, and Equinor.

CONFLICT OF INTEREST

The authors declare no conflict of interest.

ORCID

Jhabriel Varela: 0000-0003-2220-2204, Eirik Keilegavlen: 0000-0002-0333-9507, Jan M. Nordbotten: 0000-0003-1455-5704, Florin A. Radu: 0000-0002-2577-5684.

APPENDIX A: FINITE VOLUME DISCRETIZATION

This appendix deals with the discrete setting of the model. We start by introducing the partitions of the domain and then the discretized version of the equations using MPFA.

A.1 Partitions of the domain

Let $\mathcal{T}_{\Omega_i}$ and $\mathcal{T}_{\Gamma_j}$ be partitions of the subdomain Ω_i for $i \in I$ and the interface Γ_j for $j \in J$, such that $\overline{\Omega}_i = \bigcup_{K \in \mathcal{T}_{\Omega_i}} K$ and $\overline{\Gamma}_j = \bigcup_{K \in \mathcal{T}_{\Gamma_j}} K$, where all subdomain elements $K \in \mathcal{T}_{\Omega_i}$ of dimension $d_K = 2, 1, 0$, and all interface elements $K \in \mathcal{T}_{\Gamma_j}$ of dimension $d_K = 1, 0$, are required to be strictly non-overlapping simplices (see left panel of Figure A.1). We use ∂K to denote the boundary of $K \in \mathcal{T}_{\Omega_i}$, and e to denote an edge from the set of edges $\mathcal{E}_K$ of ∂K.

Since the governing equations in the fractures are given by an ODE, strictly speaking, we do not need to partition the fracture subdomains. However, since the discrete version of the interface fluxes depends on the difference between neighboring hydraulic heads, we will benefit from introducing a partition for the fractures. We will call such partition a *ghost* grid. A ghost fracture grid will allow us to associate a hydraulic head value to different heights, and thus distinguishing between "dry" and "wet" cells.

A.2 Discretization

Let us now focus on the discretization of general model problem. As mentioned in Section 3.3, we employ backward Euler to discretize the accumulation terms and MPFA-O for the spatial discretization.

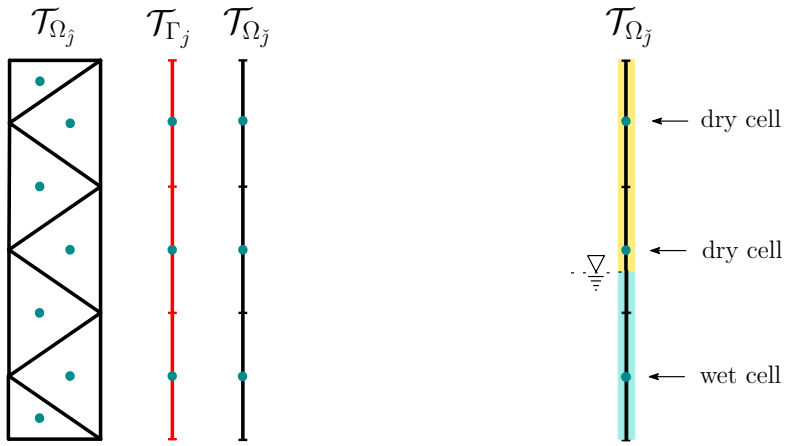

Figure A.1: Grid partitions and ghost fracture grids. Left: Coupling between a matrix grid $\mathcal{T}_{\Omega_{\hat{j}}}$, an interface grid $\mathcal{T}_{\Gamma_j}$, and a ghost fracture grid $\mathcal{T}_{\Omega_{\check{j}}}$. Right: Ghost fracture cells are employed to distinguish between dry and wet cells. We use green dots to designate the cell centers.

A.2.1 Discrete matrix equations

Let us begin with the discretization of the matrix equations. We start by integrating (17) locally:

$$\int_K \frac{\partial \theta_i}{\partial t}\,\mathrm{d}\boldsymbol{x} + \int_K \boldsymbol{\nabla}\cdot\boldsymbol{q}_i\,\mathrm{d}\boldsymbol{x} - \int_K \Psi_i\,d\boldsymbol{x} = 0, \quad \forall K \in \mathcal{T}_{\Omega_i}, i \in I, d_i = n. \tag{A1}$$

The first term of (A1) can be approximated by:

$$\int_K \frac{\partial \theta_i}{\partial t}\,\mathrm{d}\boldsymbol{x} \approx \frac{|K|}{\tau^n}\left[\theta_{i,K}^{n+1,m} + C_{i,K}^{n+1,m}\left(h_{i,K}^{n+1,m+1} - h_{i,K}^{n+1,m}\right) - \theta_{i,K}^{n}\right], \tag{A2}$$

where n and m refer, respectively, to the time and iteration levels, τ is the time step, $|K|$ is the volume of the grid cell, and $C \coloneqq \mathrm{d}\theta/\mathrm{d}\psi$ is the specific moisture capacity (Pinder & Celia, 2006).

Equation (A2) was obtained by first applying backward Euler and then Taylor-expanding $\theta_{i,K}^{n+1,m+1}$ as a function of ψ. This linearization procedure is known as *modified Picard iteration*, and it was proposed by Celia et al. (1990) as a technique to ensure mass conservation. Note that

411 other linearization techniques are also possible, see e.g., (List & Radu, 2016). The reader is
412 referred to (Varela et al., 2021) for a more detailed derivation of (A2) in the context of fixed-
413 dimensional domains.

414 Applying the divergence theorem and introducing the discrete version of Darcy's law, the
415 second term of (A1) can be estimated as

$$\begin{aligned}\int_K \boldsymbol{\nabla}\cdot\boldsymbol{q}_i \,\mathrm{d}\boldsymbol{x} = \int_{\partial K} \boldsymbol{q}_i\cdot\boldsymbol{n}_i \,\mathrm{d}S = \sum_{e\in\mathcal{E}_K} \boldsymbol{q}_{i,K,e}\cdot\boldsymbol{n}_{i,K,e}\, A_e = \sum_{e\in\mathcal{E}_K} Q_{i,K,e} \\ \approx \sum_{e\in\mathcal{E}_K}\left(k_{i,K,e}^{\mathrm{rel},n+1,m}\sum_{K'\in\mathcal{F}_{K,e}} t_{K',e}\, h_{i,K'}^{n+1,m+1}\right),\end{aligned} \tag{A3}$$

416 where A_e is the area of the edge e, $Q_{i,K,e}$ are the exact fluxes across the edges e of K, and $t_{K',e}$
417 are the transmissibility coefficients (Aavatsmark, 2002) of the edge e associated with the
418 neighboring cell K' from the set of neighboring cells $\mathcal{F}_{K,e}$.

419 Finally, the third term of (A1) can be estimated as:

$$\int_K \Psi_i \, d\boldsymbol{x} \approx |K|\Psi_{i,K}^{n+1} = F_{i,K}^{n+1}, \tag{A4}$$

420 where $F_{i,K}^{n+1}$ are the approximated integrated source terms.

421 **A.2.2 Discrete fracture equations**

422 Let us now focus on the discrete version of the fracture equations. The first term of (18)
423 can be directly approximated using backward Euler:

$$\frac{\mathrm{d}V_i}{\mathrm{d}t} \approx \frac{V_i^{n+1,m+1} - V_i^n}{\tau^n}. \tag{A5}$$

424 Note that we use V_i (not $V_{i,K}$), since this is the approximated volume of water associated with the
425 physical domain Ω_i (not a ghost cell $K \in \mathcal{T}_{\Omega_i}$).

For the second term of (18), we exploit the fact that $\Omega_i = \Gamma_j$ for $j \in \hat{S}_i$, to obtain:

$$\int_{\Omega_i} \sum_{j \in \hat{S}_i} \lambda_j \, \mathrm{d}\boldsymbol{x} = \sum_{j \in \hat{S}_i} \int_{\Omega_i} \lambda_j \, \mathrm{d}\boldsymbol{x} \approx \sum_{j \in \hat{S}_i} \sum_{K \in \mathcal{T}_{\Gamma_j}} |K| \lambda_{j,K}^{n+1,m+1} = \sum_{j \in \hat{S}_i} \sum_{K \in \mathcal{T}_{\Gamma_j}} \Lambda_{j,K}^{n+1,m+1}, \tag{A6}$$

where $\Lambda_{j,K}^{n+1,m+1}$ are the integrated mortar fluxes. Finally, the third term of (18) can be approximated via:

$$\int_{\Omega_i} \Psi_i \, \mathrm{d}\boldsymbol{x} \approx |\Omega_i| \Psi_i^{n+1} = F_i^{n+1}, \tag{A7}$$

where F_i^{n+1} is an integrated source over the subdomain Ω_i. A positive value represents irrigation whereas a negative value evaporation.

A.2.3 Discrete interface equations

Let us now deal with the discrete version of the interface law. As usual, we start integrating both sides of (21) over each interface cell:

$$\int_K \lambda_j \, \mathrm{d}\boldsymbol{x} = -\int_K \gamma_j \frac{2\kappa_j}{a_{\check{j}}} k_j^{\mathrm{rel}} \left(h_{\check{j}} - h_{\hat{j}}\right) \mathrm{d}\boldsymbol{x}, \quad \forall K \in \mathcal{T}_{\Gamma_j}, d_j = n - 1. \tag{A8}$$

The left-hand side can be estimated as:

$$\int_K \lambda_j \, \mathrm{d}\boldsymbol{x} \approx \Lambda_{j,K}^{n+1,m+1}, \tag{A9}$$

whereas the right-hand side is given by:

$$-\int_K \gamma_j \frac{2\kappa_j}{a_{\check{j}}} k_j^{\mathrm{rel}} \left(h_{\check{j}} - h_{\hat{j}}\right) \mathrm{d}\boldsymbol{x} = \gamma_{j,K} \mathcal{K}_{j,K} k_{j,K}^{\mathrm{rel},n+1,m} \left(h_{\check{j},K}^{n+1,m+1} - h_{\hat{j},K}^{n+1,m+1}\right), \tag{A10}$$

where $\mathcal{K}_{j,K} = -2|K|\kappa_{j,K} a_{j,K}^{-1}$, and $h_{\check{j},K}^{n+1,m+1}$ and $h_{\hat{j},K}^{n+1,m+1}$ are the fracture hydraulic heads from the ghost fracture grid and the adjacent matrix, respectively.

The ghost hydraulic heads are related to the physical hydraulic head such that:

$$h_{j,K}^{n+1,m+1} = \begin{cases} h_j^{n+1,m+1}, & h_j^{n+1,m+1} - z_j^{\min} > z_{j,K}, \\ z_{j,K}, & \text{otherwise} \end{cases} \quad \forall K \in \mathcal{T}_{\Omega_i}. \tag{A11}$$

The relation (A11) establishes that if the height of the water column (given by the difference between the hydraulic head of the fracture $h_j^{n+1,m+1}$ and the fractures' datum $z_j^{\min}$) exceeds the cell center height of the ghost cell $z_{j,K}$, then the ghost cell is considered "wet", and the hydraulic head corresponds to the hydraulic head of the fracture. Otherwise, the ghost cell is "dry", and its hydraulic head can be taken as the elevation head (note that here we use $\psi_{j,K} = 0$). A schematic representation of such cases is shown in the right panel of Figure A.1.

Since the discrete equations for zero-dimensional subdomains and interfaces can be trivially obtained, we do not include them here. Finally, the set of equations (A1) – (A11) must be complemented with the discretized version of the boundary conditions. Neumann (24) and Dirichlet (25) boundary conditions are treated in the classical way. For the internal boundary conditions (23), we require the integrated fluxes on the internal boundaries to match the integrated interface fluxes.

APPENDIX B: TIME-STEPPING ALGORITHM

The time-stepping algorithm follows closely the one from HYDRUS-1D (Šimůnek et al., 2005) and employed in (Varela et al., 2021). In Figure B.1, we show the complete flowchart as it is implemented in `PorePy`. The main idea is to select the time step based on the number of iterations needed to reach convergence in the previous time level. If the number of iterations is lower than a prescribed value `iter_low`, the time step can be relaxed by multiplying it by an overrelaxation factor `over_relax_factor > 1`. On the other hand, if the number of iterations

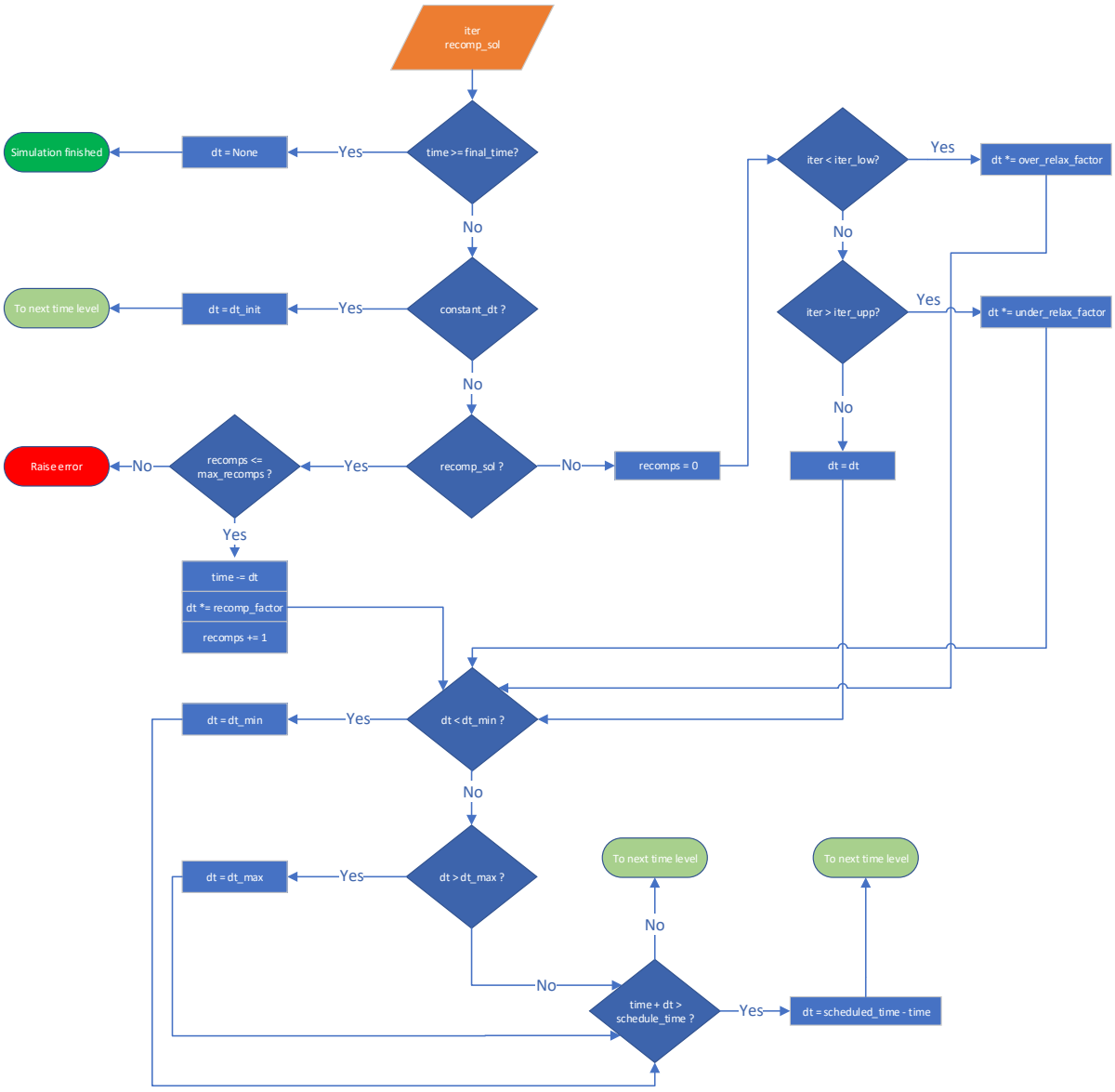

Figure B.1: Flowchart of the time-stepping algorithm employed to solve the discretized system of non-linear algebraic equations.

is larger than a prescribed value `iter_upp`, the time step is restricted by multiplying it by an underrelaxation factor `under_relax_factor < 1`. If the number of iterations lies between `iter_low` and `iter_upp`, the time step remains the same.

The time step is constrained between a prescribed range [`dt_min, dt_max`]. Moreover, we allow for the possibility of re-computing the solution for a given time level with a smaller

time step. This is done by multiplying the time step by a re-computation factor `recomp_factor < 1`. In our context, this functionality is used when convergence is achieved but a non-physical solution is obtained, e.g., negative volume is encountered for a given time step or when the solution diverges.

APPENDIX C: EXACT SOLUTIONS FOR THE CONVERGENCE ANALYSIS

To derive the manufactured solution from Section 4.1, we follow closely the procedure presented by Varela et al. (2022). The mixed-dimensional domain consists of a matrix and a single vertical fracture of length 0.5 fully embedded in the middle of the domain. First, we divide the bulk subdomain Ω_2 into three parts, namely $\Omega_2 = \Omega_2^{\text{bot}} \cup \Omega_2^{\text{mid}} \cup \Omega_2^{\text{top}}$, such that:

$$\Omega_2^{\text{bot}} \coloneqq \{\boldsymbol{x} \in \Omega_2 : z < 0.25\}, \tag{C1}$$

$$\Omega_2^{\text{mid}} \coloneqq \{\boldsymbol{x} \in \Omega_2 : 0.25 \leq z \leq 0.75\}, \tag{C2}$$

$$\Omega_2^{\text{top}} \coloneqq \{\boldsymbol{x} \in \Omega_2 : z > 0.75\}. \tag{C3}$$

Let us now define the spatial function $\delta(\boldsymbol{x})$ measuring the shortest distance from any point in the matrix to the fracture:

$$\delta(\boldsymbol{x}) \coloneqq \begin{cases} [(x-0.5)^2 + (z-0.25)^2]^{0.5}, & \boldsymbol{x} \in \Omega_2^{\text{bot}} \\ [(x-0.5)^2]^{0.5}, & \boldsymbol{x} \in \Omega_2^{\text{mid}} \\ [(x-0.5)^2 + (z-0.75)^2]^{0.5}, & \boldsymbol{x} \in \Omega_2^{\text{top}} \end{cases}. \tag{C4}$$

Furthermore, consider the bubble function $\omega(\boldsymbol{x})$ defined for all $\boldsymbol{x} \in \Omega_2^{\text{mid}}$ and given by

$$\omega(\boldsymbol{x}) \coloneqq (z-0.25)^2(z-0.75)^2. \tag{C5}$$

Now, we define the hydraulic head in the bulk $h_2(\boldsymbol{x}, t)$ for all $t \in (0, T) = (0, 0.5)$ as:

$$h_b(\boldsymbol{x}, t) \coloneqq \begin{cases} t\delta^{2.5} + 0.75, & \boldsymbol{x} \in \Omega_b \setminus \Omega_b^{\text{mid}} \\ t(\delta^{2.5} + \omega\delta) + 0.75, & \boldsymbol{x} \in \Omega_b^{\text{mid}} \end{cases}, \tag{C6}$$

This choice of hydraulic head distribution in the bulk ensures saturated conditions in Ω_2^{mid} during the simulation time. Now, the pressure head can be easily computed via:

$$\psi_2(\boldsymbol{x}, t) = h_2(\boldsymbol{x}, t) - z. \tag{C7}$$

For the sake of simplicity, we do not employ the van Genuchten-Mualem relations. Instead, we define simpler expressions similar to those employed by Radu and Wang (2014):

$$\theta_b(\boldsymbol{x}, t) = \begin{cases} (1 - \psi_b)^{-1}, & \psi_b < 0 \\ 1, & \psi_b \geq 0 \end{cases}, \tag{C8}$$

$$k_b^{\mathrm{rel}}(\boldsymbol{x}, t) = \begin{cases} \exp(\psi_b) & \psi_b < 0 \\ 1 & \psi_b \geq 0 \end{cases}. \tag{C9}$$

By setting $\boldsymbol{K}_b = \boldsymbol{I}$ and using (C7) and (C9) , the Darcy flux $\boldsymbol{q}_b(\boldsymbol{x}, t)$ is set via Eq. (2). Moreover, by computing the accumulation term $\partial\theta_b/\partial t$ using (C8) and applying the mass conservation equation (1), we obtain the source term in the matrix $\Psi_2(\boldsymbol{x}, t)$.

With $\boldsymbol{q}_b(\boldsymbol{x}, t)$ available, it can be checked via (3) that the interface fluxes at each side of the fracture satisfy:

$$\lambda_j(z, t) = t\omega(z), \quad j = \{1, 2\}. \tag{C10}$$

The interface fluxes are positive for $t > 0$, resulting in imbibition of water in the fracture. Recall that the choice of h_2 ensures $\gamma_1 = \gamma_2 = 1$ at all times.

Setting $a_f = 0.01$, the normal permeabilities κ_1 and κ_2 on the interfaces are constrained via (9) and given by:

$$\kappa_j(z, t) = 0.005t \frac{\omega(z)}{(0.75 - z)}, \quad j = \{1, 2\}. \tag{C11}$$

The fact that the normal permeability is time-dependent is a mathematical consequence of the manufactured solution and is not the case for the physical model.

491 Without external sources and assuming an initially dry fracture, the volume of water
492 $V_1(t)$ can be obtained by solving the initial value problem (7) — (8) exactly:

$$V_1(t) = t^2 \int_{0.25}^{0.75} \omega(z)\, \mathrm{d}z\,, \quad V_1(0) = 0. \tag{C12}$$

493 The hydraulic head in the fracture $h_1(t)$ can now be obtained by inverting the volume
494 integral (14), which in the case of constant aperture is simply given by:

$$h_f(t) = a_f^{-1} V_f(t) + 0.25. \tag{C13}$$

495 The first term of (C13) represents the height of the local water column, whereas the
496 second term considers the correction based on the fractures' datum. Finally, we require initial
497 interface fluxes to satisfy (C10) and initial and boundary hydraulic heads to satisfy (C7) with
498 Dirichlet conditions.

499 **REFERENCES**
500

501 Aavatsmark, I. (2002). An introduction to multipoint flux approximations for quadrilateral grids.
502 *Computational Geosciences*, *6*, 405-432. https://doi.org/10.1023/A:1021291114475

503 Ahmed, E., Jaffré, J., & Roberts, J. E. (2017). A reduced fracture model for two-phase flow with
504 different rock types. *Mathematics and Computers in Simulation*, *137*, 49-70.
505 https://doi.org/10.1016/j.matcom.2016.10.005

506 Berre, I., Doster, F., & Keilegavlen, E. (2019). Flow in fractured porous media: A review of
507 conceptual models and discretization approaches. *Transport in Porous Media*, *130*(1),
508 215-236. https://doi.org/10.1007/s11242-018-1171-6

509 Boon, W. M., Nordbotten, J. M., & Vatne, J. E. (2021). Functional analysis and exterior calculus
510 on mixed-dimensional geometries. *Annali di Matematica Pura ed Applicata (1923-)*,
511 *200*(2), 757-789. https://doi.org/10.1007/s10231-020-01013-1

512 Boon, W. M., Nordbotten, J. M., & Yotov, I. (2018). Robust discretization of flow in fractured
513 porous media. *SIAM Journal on Numerical Analysis*, *56*(4), 2203-2233.
514 https://doi.org/10.1137/17M1139102

515 Brouyère, S. (2006). Modelling the migration of contaminants through variably saturated dual-
516 porosity, dual-permeability chalk. *Journal of Contaminant Hydrology*, *82*(3-4), 195-219.
517 https://doi.org/10.1016/j.jconhyd.2005.10.004

Carsel, R. F., & Parrish, R. S. (1988). Developing joint probability distributions of soil water retention characteristics. *Water Resources Research*, *24*(5), 755-769. https://doi.org/10.1029/WR024i005p00755

Celia, M. A., Bouloutas, E. T., & Zarba, R. L. (1990). A general mass-conservative numerical solution for the unsaturated flow equation. *Water Resources Research*, *26*(7), 1483-1496. https://doi.org/10.1029/WR026i007p01483

Chan, T. F., & Vese, L. A. (2001). Active contours without edges. *IEEE Transactions on image processing*, *10*(2), 266-277. https://doi.org/10.1109/83.902291

Chen, Y.-F., Ye, Y., Hu, R., Yang, Z., & Zhou, C.-B. (2022). Modeling unsaturated flow in fractured rocks with scaling relationships between hydraulic parameters. *Journal of Rock Mechanics and Geotechnical Engineering*, *14*(6), 1697-1709. https://doi.org/10.1016/j.jrmge.2022.02.008

Chen, Z., Huan, G., & Ma, Y. (2006). *Computational methods for multiphase flows in porous media*. SIAM. https://doi.org/10.1137/1.9780898718942

Dragila, M. I., & Wheatcraft, S. W. (2001). Free-surface films. In *Conceptual models of flow and transport in the fractured vadose zone* (pp. 217-241). National Research Council, National Academy Press. https://doi.org/10.17226/10102

Farthing, M. W., & Ogden, F. L. (2017). Numerical solution of Richards' equation: A review of advances and challenges. *Soil Science Society of America Journal*, *81*(6), 1257-1269. https://doi.org/10.2136/sssaj2017.02.0058

Formaggia, L., Fumagalli, A., & Scotti, A. (2021). Numerical Methods for Flow in Fractured Porous Media. In *Encyclopedia of Solid Earth Geophysics* (pp. 1125-1130). Springer International Publishing. https://doi.org/10.1007/978-3-030-58631-7_289

Keilegavlen, E., Berge, R., Fumagalli, A., Starnoni, M., Stefansson, I., Varela, J., & Berre, I. (2021). Porepy: An open-source software for simulation of multiphysics processes in fractured porous media. *Computational Geosciences*, *25*, 243-265. https://doi.org/10.1007/s10596-020-10002-5

Klausen, R. A., Radu, F. A., & Eigestad, G. T. (2008). Convergence of MPFA on triangulations and for Richards' equation. *International journal for numerical methods in fluids*, *58*(12), 1327-1351. https://doi.org/10.1002/fld.1787

Koohbor, B., Fahs, M., Hoteit, H., Doummar, J., Younes, A., & Belfort, B. (2020). An advanced discrete fracture model for variably saturated flow in fractured porous media. *Advances in Water Resources*, *140*, 103602. https://doi.org/10.1016/j.advwatres.2020.103602

Kordilla, J., Sauter, M., Reimann, T., & Geyer, T. (2012). Simulation of saturated and unsaturated flow in karst systems at catchment scale using a double continuum approach. *Hydrology and Earth System Sciences*, *16*(10), 3909-3923. https://doi.org/10.5194/hess-16-3909-2012

555 Kumar, K., List, F., Pop, I. S., & Radu, F. A. (2020). Formal upscaling and numerical validation
556 of unsaturated flow models in fractured porous media. *Journal of Computational Physics*,
557 *407*, 109138. https://doi.org/10.1016/j.jcp.2019.109138

558 Kuráž, M., Mayer, P., Lepš, M., & Trpkošová, D. (2010). An adaptive time discretization of the
559 classical and the dual porosity model of Richards' equation. *Journal of computational*
560 *and applied mathematics*, *233*(12), 3167-3177. https://doi.org/10.1016/j.cam.2009.11.056

561 Li, X., & Li, D. (2019). A numerical procedure for unsaturated seepage analysis in rock mass
562 containing fracture networks and drainage holes. *Journal of hydrology*, *574*, 23-34.
563 https://doi.org/10.1016/j.jhydrol.2019.04.014

564 List, F., Kumar, K., Pop, I. S., & Radu, F. A. (2020). Rigorous upscaling of unsaturated flow in
565 fractured porous media. *SIAM Journal on Mathematical Analysis*, *52*(1), 239-276.
566 https://doi.org/10.1137/18M1203754

567 List, F., & Radu, F. A. (2016). A study on iterative methods for solving Richards' equation.
568 *Computational Geosciences*, *20*, 341-353. https://doi.org/10.1007/s10596-016-9566-3

569 Macfarlane, A., & Ewing, R. C. (2006). *Uncertainty underground: Yucca Mountain and the*
570 *nation's high-level nuclear waste*. MIT press.
571 https://doi.org/10.7551/mitpress/6965.001.0001

572 Martin, V., Jaffré, J., & Roberts, J. E. (2005). Modeling fractures and barriers as interfaces for
573 flow in porous media. *SIAM Journal on Scientific Computing*, *26*(5), 1667-1691.
574 https://doi.org/10.1137/S1064827503429363

575 Mualem, Y. (1976). A new model for predicting the hydraulic conductivity of unsaturated porous
576 media. *Water Resources Research*, *12*(3), 513-522.
577 https://doi.org/10.1029/WR012i003p00513

578 Nordbotten, J. M., & Keilegavlen, E. (2021). An introduction to multi-point flux (MPFA) and
579 stress (MPSA) finite volume methods for thermo-poroelasticity. In *Polyhedral Methods*
580 *in Geosciences* (pp. 119-158). Springer. https://doi.org/10.1007/978-3-030-69363-3_4

581 Pinder, G. F., & Celia, M. A. (2006). *Subsurface hydrology*. John Wiley & Sons.

582 Radu, F. A., & Wang, W. (2014). Convergence analysis for a mixed finite element scheme for
583 flow in strictly unsaturated porous media. *Nonlinear Analysis: Real World Applications*,
584 *15*, 266-275. https://doi.org/10.1016/j.nonrwa.2011.05.003

585 Richards, L. A. (1931). Capillary conduction of liquids through porous mediums. *Physics*, *1*(5),
586 318-333. https://doi.org/10.1063/1.1745010

587 Robineau, T., Tognelli, A., Goblet, P., Renard, F., & Schaper, L. (2018). A double medium
588 approach to simulate groundwater level variations in a fissured karst aquifer. *Journal of*
589 *hydrology*, *565*, 861-875. https://doi.org/10.1016/j.jhydrol.2018.09.002

590 Scudeler, C., Paniconi, C., Pasetto, D., & Putti, M. (2017). Examination of the seepage face
591 boundary condition in subsurface and coupled surface/subsurface hydrological models.
592 *Water Resources Research*, *53*(3), 1799-1819. https://doi.org/10.1002/2016WR019277

593 Šimůnek, J., & Bradford, S. A. (2008). Vadose zone modeling: Introduction and importance.
594 *Vadose Zone Journal*, *7*(2), 581-586. https://doi.org/10.2136/vzj2008.0012

595 Šimůnek, J., Van Genuchten, M. T., & Sejna, M. (2005). The HYDRUS-1D software package
596 for simulating the one-dimensional movement of water, heat, and multiple solutes in
597 variably-saturated media. *University of California-Riverside Research Reports*, *3*, 1-240.

598 Spiridonov, D., Vasilyeva, M., & Chung, E. T. (2020). Generalized Multiscale Finite Element
599 method for multicontinua unsaturated flow problems in fractured porous media. *Journal*
600 *of computational and applied mathematics*, *370*, 112594.
601 https://doi.org/10.1016/j.cam.2019.112594

602 Su, G. W., Nimmo, J. R., & Dragila, M. I. (2003). Effect of isolated fractures on accelerated flow
603 in unsaturated porous rock. *Water Resources Research*, *39*(12).
604 https://doi.org/10.1029/2002WR001691

605 Therrien, R., & Sudicky, E. A. (1996). Three-dimensional analysis of variably-saturated flow
606 and solute transport in discretely-fractured porous media. *Journal of Contaminant*
607 *Hydrology*, *23*(1-2), 1-44. https://doi.org/10.1016/0169-7722(95)00088-7

608 Tokunaga, T. K., & Wan, J. (1997). Water film flow along fracture surfaces of porous rock.
609 *Water Resources Research*, *33*(6), 1287-1295. https://doi.org/10.1029/97WR00473

610 Tokunaga, T. K., & Wan, J. (2001). Approximate boundaries between different flow regimes in
611 fractured rocks. *Water Resources Research*, *37*(8), 2103-2111.
612 https://doi.org/10.1029/2001WR000245

613 Tokunaga, T. K., Wan, J., & Sutton, S. R. (2000). Transient film flow on rough fracture surfaces.
614 *Water Resources Research*, *36*(7), 1737-1746. https://doi.org/10.1029/2000WR900079

615 Tran, L. K., & Matthai, S. K. (2021). Simulation of the Infiltration of Fractured Rock in the
616 Unsaturated Zone. *Applied Sciences*, *11*(19), 9148. https://doi.org/10.3390/app11199148

617 Trémolières, R., Lions, J. L., & Glowinski, R. (2011). *Numerical analysis of variational*
618 *inequalities*. Elsevier.

619 Van Genuchten, M. T. (1980). A closed-form equation for predicting the hydraulic conductivity
620 of unsaturated soils. *Soil Science Society of America Journal*, *44*(5), 892-898.
621 https://doi.org/10.2136/sssaj1980.03615995004400050002x

622 Varela, J. (2023). *unsat-frac v2.0.0-alpha*. In https://doi.org/10.5281/zenodo.8083174.

Varela, J., Ahmed, E., Keilegavlen, E., Nordbotten, J. M., & Radu, F. A. (2022). A posteriori error estimates for hierarchical mixed-dimensional elliptic equations. *Journal of Numerical Mathematics*. https://doi.org/10.1515/jnma-2022-0038

Varela, J., Gasda, S. E., Keilegavlen, E., & Nordbotten, J. M. (2021). A Finite-Volume-Based Module for Unsaturated Poroelasticity. In K.-A. Lie & O. Møyner (Eds.), *Advanced Modeling with the MATLAB Reservoir Simulation Toolbox*. Cambridge University Press. https://doi.org/10.1017/9781009019781.019

Wang, J. S. Y., & Narasimhan, T. N. (1985). Hydrologic mechanisms governing fluid flow in a partially saturated, fractured, porous medium. *Water Resources Research*, *21*(12), 1861-1874. https://doi.org/10.1029/WR021i012p01861

Wang, Y., Ma, J., Zhang, Y., Zhao, M., & Edmunds, W. M. (2013). A new theoretical model accounting for film flow in unsaturated porous media. *Water Resources Research*, *49*(8), 5021-5028. https://doi.org/10.1002/wrcr.20390

White, F. M. (2006). *Viscous Fluid Flow* (3 ed.). McGraw-Hill Education.